Calculation of model Hamiltonian parameters for $LaMnO_3$ using maximally localized Wannier functions

Roman Kováčik* and Claude Ederer
School of Physics, Trinity College Dublin, Dublin 2, Ireland
(Received 17 December 2009; revised manuscript received 7 May 2010; published 8 June 2010)

In this work we demonstrate that maximally localized Wannier functions (MLWFs) based on Kohn-Sham band structures provide a very robust and systematic way to construct realistic, materials-specific tight-binding models for further theoretical analysis. In particular, we construct MLWFs for the Mn e_g bands in $LaMnO_3$, and we monitor changes in the MLWF matrix elements induced by different magnetic configurations and structural distortions. By comparing our results with commonly used model Hamiltonians for manganites, where electrons can hop between two "e_g-like" orbitals located on each Mn site, we obtain values for the local Jahn-Teller and Hund's rule coupling strength, the hopping amplitudes between all nearest and further neighbors, and the corresponding reduction due to the $GdFeO_3$-type distortion. In addition, our analysis allows us to systematically assess and quantify the limitations of such an effective e_g-band description. We find that the most crucial limitation of such models stems from neglecting changes in the underlying Mn(d)-O(p) hybridization, which not only lead to a significant difference in hopping for (local) spin majority/minority electrons but also to a nonlocal effect of the Jahn-Teller distortion and a significant reduction in the local Jahn-Teller coupling strength due to the $GdFeO_3$-type distortion.

DOI: 10.1103/PhysRevB.81.245108 PACS number(s): 75.47.Lx, 71.70.Ej, 71.10.−w

I. INTRODUCTION

The theoretical description of complex transition-metal oxides and similar materials is very often based on effective tight-binding (TB) models, i.e., a representation of the electronic structure within a certain energy region in terms of localized atomiclike orbitals. Simplified TB models with a small number of orbitals can be used to study the essential mechanisms governing complex physical behavior.[1–4]

The electronic properties of colossal magnetoresistive manganites, $R_{1-x}A_xMnO_3$ (R: trivalent rare-earth cation and A: divalent alkaline earth cation), are often described within an effective "two-band" TB model, where electrons can hop between the two e_g levels on each Mn site. The corresponding Hamiltonian typically also contains several local terms describing the coupling of the e_g states to the t_{2g} core spin, to the Jahn-Teller (JT) distortion of the oxygen octahedra, and/or the electron-electron Coulomb repulsion. It has recently been shown, that such a model (with parameters obtained partly from first-principles calculations and partly by fitting to experimental data) is able to reproduce the basic structure of the phase diagram as a function of doping and temperature found in manganite systems such as $La_{1-x}(Ca,Sr)_xMnO_3$.[4]

The construction of localized Wannier orbitals from the Kohn-Sham states calculated using density-functional theory (DFT) represents an elegant and systematic way to obtain realistic (materials-specific) TB models.[5–12] DFT calculations are known to give a realistic description of electronic structure for systems where electronic correlation effects are not too strong.[13,14] Furthermore, for materials where correlation effects are important, a Wannier representation of the Kohn-Sham band structure can be used to define a subset of orbitals (the "correlated subspace"), which can then be used as basis for a more elaborate treatment of correlation effects beyond standard DFT. This is done, for example, in DFT+DMFT (DMFT=dynamical mean-field theory) calculations,[8,9,12,15–17] which aim at an accurate quantitative description of materials where electronic correlation cannot be ignored.

Several different ways to obtain Wannier functions for the relevant electronic degrees of freedom have been employed previously, including the construction of maximally localized Wannier functions (MLWFs),[9,18–20] orthogonalized projections of specific atomic orbitals on the Bloch functions within a certain energy window,[6,8,11,12] and downfolded Nth-order muffin-tin orbitals.[7,9,21,22]

In this work we construct MLWFs corresponding to the Mn e_g states for $LaMnO_3$, the parent compound for many manganite systems, based on DFT calculations within the generalized gradient approximation (GGA). We calculate the real-space Hamiltonian matrix elements in the MLWF basis for different structural modifications and for different magnetic configurations and we compare the obtained results with assumptions made in commonly used two band TB models for manganites.[2,4]

A number of previous studies have used DFT calculations to obtain parameters of typical effective e_g Hamiltonians for manganite systems.[11,23–25] In most of these cases the Kohn-Sham band structure was used as reference for the "noninteracting" part of the corresponding model Hamiltonian, and different fitting procedures to obtain the hopping amplitudes, Hund's rule coupling, and Jahn-Teller splitting have been employed. In contrast, in Ref. 11 the full interacting Hamiltonian (in mean-field approximation) has been fitted using Wannier functions obtained from LDA+U calculations.

The analysis presented here is closely related to Ref. 25, which examined the validity of the two band picture by fitting TB model parameters (including the hopping between nearest and next-nearest neighbors) to the DFT band structure obtained within the local spin density approximation (LSDA). In Ref. 25 the effects of magnetic ordering, Jahn-

Teller, and $GdFeO_3$ distortions were analyzed separately, to allow for an independent determination of the various model parameters. A similar strategy is followed here. However, the approach based on MLWFs used in the present work is less biased and more generally applicable and thus allows for a more systematic analysis of the TB parameters than the various fitting procedures employed in previous works.[11,23–25] The MLWF approach automatically leads to a TB parameterization of the relevant bands so that the parameters of the model can simply be "read off" and no fitting procedure is required. This allows to clearly identify potential discrepancies between a simplified model and the full DFT band structure. The MLWF approach is also well suited for the construction of the correlated orbital subspace used for DFT +DMFT calculations.[9]

This paper is organized as follows. In the following section we describe the theoretical background of our work. Thereby, Sec. II A summarizes the effective two band model that is often used for a theoretical treatment of manganites, Sec. II B presents the definition of the MLWFs, Sec. II C describes the various structural modifications of $LaMnO_3$ investigated throughout this work and Sec. II D lists some of the calculational details. The presentation of results starts with the case of the ideal cubic perovskite structure in Sec. III A. The individual effects of the staggered JT and the $GdFeO_3$-type (GFO) distortions are then presented in Secs. III B and III C, respectively. This is followed by the results for the combined distortion in Sec. III D and the construction of a refined TB model and its application to the full experimental structure of $LaMnO_3$ in Sec. III E. Finally, the most important results and conclusions are summarized in Sec. IV.

II. METHOD AND THEORETICAL BACKGROUND

A. Effective two-band models for $LaMnO_3$

$LaMnO_3$ crystallizes in an orthorhombically distorted perovskite structure with *Pbnm* space group [see Fig. 1v] and *A*-type antiferromagnetic (A-AFM) order of the magnetic moments of the Mn cations.[27,28] The deviation from the simple cubic perovskite structure [Fig. 1i] can be decomposed into a staggered JT distortion of the MnO_6 octahedra within the *x*-*y* plane [Fig. 1ii], the so-called GFO distortion, consisting of collective tiltings and rotations of the oxygen octahedra [Fig. 1iii], and "the rest," i.e., displacements of the La cations from their ideal positions plus a homogeneous orthorhombic strain [Fig. 1v].[25]

The electronic structure of $LaMnO_3$ close to the Fermi energy is dominated by Mn $3d$ states, which are split by the cubic component of the crystal field into the lower-lying threefold degenerate t_{2g} and the higher-lying twofold degenerate e_g states.[25,29,30] The formal electronic configuration Mn^{3+}:$[Ar]3d^4$ leads to a high spin state of the Mn cation with fully occupied local majority spin t_{2g} states and one electron per local majority spin e_g state while both t_{2g} and e_g minority spin states are empty.

Based on this electronic structure, the theoretical description of manganites often employs an effective two-band TB picture, where electrons can hop between the two e_g levels on each Mn site. This hopping is facilitated by hybridization

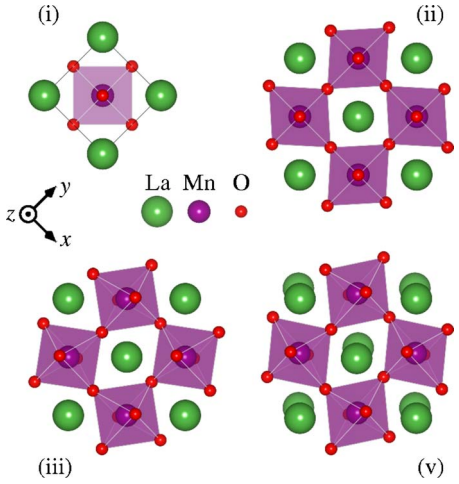

FIG. 1. (Color online) Different structural modifications of $LaMnO_3$ investigated in this work, viewed along the [001] direction: (i) ideal cubic perovskite, (ii) purely Jahn-Teller distorted, (iii) purely $GdFeO_3$-type distorted, and (v) experimental *Pbnm* structure. Pictures have been generated using VESTA (Ref. 26).

with the oxygen $2p$ states, which, however, are not explicitly included in the TB model. It is therefore understood, that the "atomic" e_g states used in the TB model are indeed somewhat extended Wannier orbitals that also include the hybridization with the O $2p$ states. In contrast, the three t_{2g} electrons are assumed to be tightly bound to a specific Mn site where they give rise to a local "core spin" $S=3/2$. This core spin then interacts with the valence e_g electron spin via Hund's rule coupling. In addition, a JT distortion of the surrounding oxygen octahedron splits the two e_g levels on the corresponding Mn site whereas elastic coupling between neighboring oxygen octahedra gives rise to a cooperative effect. The GFO distortion in this picture is usually assumed to simply reduce the effective hopping amplitudes between neighboring Mn sites due to the resulting nonideal Mn-O-Mn bond angle. In addition, a local electron-electron interaction between electrons occupying the same Mn site can be included in the model.[2,4]

The electronic Hamiltonian for such a model can be expressed as

$$\hat{H} = \hat{H}_{\text{kin}} + \hat{H}_{\text{local}}, \tag{1}$$

where

$$\hat{H}_{\text{kin}} = \sum_{a,b,\mathbf{R},\Delta\mathbf{R},\sigma} t_{ab}(\Delta\mathbf{R})\hat{c}^{\dagger}_{b(\mathbf{R}+\Delta\mathbf{R})\sigma}\hat{c}_{a\mathbf{R}\sigma} + \text{H.c.} \tag{2}$$

describes the electron hopping between orbital $|a\rangle$ (spin σ) at site $\mathbf{R}$ and orbital $|b\rangle$ at site $\mathbf{R}+\Delta\mathbf{R}$ and it is assumed that all sites are translationally equivalent so that the hopping amplitudes $t_{ab}(\Delta\mathbf{R})$ depend only on the relative position between the two sites.

Representing the e_g orbital subspace within the usual basis $|1\rangle=|3z^2-r^2\rangle$ and $|2\rangle=|x^2-y^2\rangle$, and assuming cubic symmetry, the nearest-neighbor hopping along the three Cartesian directions has the following form:

$$\mathbf{t}(\pm a_c\hat{\mathbf{z}}) = \begin{pmatrix} t & 0 \\ 0 & t' \end{pmatrix}, \tag{3}$$

$$\mathbf{t}(\pm a_c\hat{\mathbf{x}}) = t\begin{pmatrix} \frac{1}{4} & -\frac{\sqrt{3}}{4} \\ -\frac{\sqrt{3}}{4} & \frac{3}{4} \end{pmatrix} + t'\begin{pmatrix} \frac{3}{4} & \frac{\sqrt{3}}{4} \\ \frac{\sqrt{3}}{4} & \frac{1}{4} \end{pmatrix}, \tag{4}$$

$$\mathbf{t}(\pm a_c\hat{\mathbf{y}}) = t\begin{pmatrix} \frac{1}{4} & \frac{\sqrt{3}}{4} \\ \frac{\sqrt{3}}{4} & \frac{3}{4} \end{pmatrix} + t'\begin{pmatrix} \frac{3}{4} & -\frac{\sqrt{3}}{4} \\ -\frac{\sqrt{3}}{4} & \frac{1}{4} \end{pmatrix}. \tag{5}$$

Here, a_c is the lattice constant of the underlying cubic perovskite structure. The hopping t' between two neighboring $|x^2-y^2\rangle$-type orbitals along $\hat{\mathbf{z}}$ is small due to the planar shape of this orbital and it is therefore often neglected. In this case, the nearest-neighbor hopping depends only on a single parameter t, the hopping along $\hat{\mathbf{z}}$ between $|3z^2-r^2\rangle$-type orbitals.

$\hat{H}_{\text{local}}$ contains all local interaction terms included in the model, i.e., Hund's rule coupling with the t_{2g} core spin, the JT coupling to the oxygen octahedra distortion, and eventually also the electron-electron interaction. In this work we will use the GGA Kohn-Sham band structure as reference for the noninteracting part of the Hamiltonian (similar to Refs. 23–25, and in the same spirit as in the DFT+U and DFT+DMFT approaches, see, e.g., Refs. 9, 16, 17, and 31), i.e., we will discuss only the Hund's rule and JT coupling. We note that this does not imply that the electron-electron interaction is unimportant for the physics of $LaMnO_3$. In fact it has been argued in Ref. 11 that the electron-electron interaction in $LaMnO_3$ is comparable in strength to the JT coupling. The Hund's rule and JT coupling terms considered here are of the form

$$\hat{H}_{\text{Hund}} = -J\sum_{\mathbf{R}} \mathbf{S}_{\mathbf{R}} \cdot \mathbf{s}_{\mathbf{R}} \tag{6}$$

and

$$\hat{H}_{\text{JT}} = -\lambda \sum_{\mathbf{R},\sigma,a,b} \hat{c}^{\dagger}_{a\mathbf{R}\sigma}(Q^x_{\mathbf{R}}\tau^x_{ab} + Q^z_{\mathbf{R}}\tau^z_{ab})\hat{c}_{b\mathbf{R}\sigma}. \tag{7}$$

Here, J is the Hund's rule coupling strength and $\mathbf{S}_{\mathbf{R}}$ is the t_{2g} core spin at site $\mathbf{R}$, which in the following we will consider as classical vector normalized to $|\mathbf{S}_{\mathbf{R}}|=1$. $\mathbf{s}_{\mathbf{R}} = \Sigma_{a,\sigma,\sigma'} c^{\dagger}_{a\mathbf{R}\sigma}\boldsymbol{\tau}_{\sigma\sigma'}c_{a\mathbf{R}\sigma'}$ is the corresponding e_g valence spin, λ describes the strength of the JT coupling, and $\boldsymbol{\tau}_{\sigma\sigma'}$ are the usual Pauli matrices. The quantities $Q^x_{\mathbf{R}}$ and $Q^z_{\mathbf{R}}$ describe the JT distortion of the oxygen octahedron surrounding site $\mathbf{R}$

$$Q^x_{\mathbf{R}} = \frac{1}{2\sqrt{2}}(d^x_{\mathbf{R}} - d^y_{\mathbf{R}}), \tag{8}$$

$$Q^z_{\mathbf{R}} = \frac{1}{2\sqrt{6}}(2d^z_{\mathbf{R}} - d^x_{\mathbf{R}} - d^y_{\mathbf{R}}), \tag{9}$$

where $d^x_{\mathbf{R}}$, $d^y_{\mathbf{R}}$, and $d^z_{\mathbf{R}}$ indicate the O-O distances along the x, y, and z directions, corresponding to the oxygen octahedron located at site $\mathbf{R}$.

B. Maximally localized Wannier functions

As is well known from basic solid-state physics, the eigenfunctions within a periodic crystal potential are extended Bloch waves, classified by a wave-vector $\mathbf{k}$ and a band-index m. These Bloch waves can in turn be expressed as a Bloch sum of "atomiclike" localized TB basis functions or *Wannier functions*. For an isolated group of N Bloch states $|\psi_{m\mathbf{k}}\rangle$, i.e., a group of bands that are energetically separated from all lower- or higher-lying bands throughout the entire Brillouin zone (BZ), a set of N localized Wannier functions $|w_{n\mathbf{T}}\rangle$, associated with lattice vector $\mathbf{T}$, is defined via the following transformation:[18,19]

$$|w_{n\mathbf{T}}\rangle = \frac{V}{(2\pi)^3}\int_{\text{BZ}}\left[\sum_{m=1}^{N} U^{(\mathbf{k})}_{mn}|\psi_{m\mathbf{k}}\rangle\right]e^{-i\mathbf{k}\cdot\mathbf{T}}d\mathbf{k}. \tag{10}$$

Here, $\mathbf{U}^{(\mathbf{k})}$ is a unitary matrix mixing Bloch states at wave-vector $\mathbf{k}$. Different $\mathbf{U}^{(\mathbf{k})}$ lead to different Wannier orbitals, which are not uniquely determined by Eq. (10). However, Marzari and Vanderbilt showed that a unique set of MLWFs can be obtained by minimizing the total quadratic spread of the Wannier orbitals, defined as[18]

$$\Omega = \sum_{n}^{N}[\langle r^2\rangle_n - \langle \mathbf{r}\rangle_n^2], \tag{11}$$

where $\langle\hat{O}\rangle_n = \langle w_{n0}|\hat{O}|w_{n0}\rangle$.

For the case of entangled Bloch bands, i.e., bands that are not energetically separated from other groups of higher- or lower-lying states, an energy window $[E_{\min}, E_{\max}]$ can be defined such that there are $N^{(\mathbf{k})}_{\text{win}} \geqslant N$ Bloch bands within the energy window at each $\mathbf{k}$ vector, and then an N-dimensional manifold of mixed Bloch states is obtained as[19]

$$|\psi^{\text{dis}}_{m\mathbf{k}}\rangle = \sum_{l\in N^{(\mathbf{k})}_{\text{win}}} U^{\text{dis}(\mathbf{k})}_{lm}|\psi_{l\mathbf{k}}\rangle. \tag{12}$$

The corresponding Wannier functions can then be obtained from the mixed Bloch states by replacing $|\psi_{m\mathbf{k}}\rangle$ with $|\psi^{\text{dis}}_{m\mathbf{k}}\rangle$ in Eq. (10). The unitary rectangular $N^{(\mathbf{k})}_{\text{win}}\times N$ matrix $\mathbf{U}^{\text{dis}(\mathbf{k})}$ is also uniquely determined by the condition of maximal localization, i.e., it can be obtained by minimizing $\Omega(\mathbf{U}^{(\mathbf{k})}, \mathbf{U}^{\text{dis}(\mathbf{k})})$.[19]

A starting value for the unitary matrix $\mathbf{U}^{(\mathbf{k})}\cdot\mathbf{U}^{\text{dis}(\mathbf{k})}$ is usually obtained by projecting a set of localized trial orbitals $|g_m\rangle$ on the Bloch states within the chosen energy window

$$|\phi_{m\mathbf{k}}\rangle = \sum_{l\in N^{(\mathbf{k})}_{\text{win}}} |\psi_{l\mathbf{k}}\rangle\langle\psi_{l\mathbf{k}}|g_m\rangle \tag{13}$$

and subsequent orthogonalization

TABLE I. Wyckoff parameters of the O(4c), $(x, y, 0.25)$, O(8d), (x,y,z), and La(4c), $(x, y, 0.25)$, sites for the various structural configurations used in this work (compare with Table I in Ref. 25).

		Expt. (Ref. 32)	(ii)	(iii)	(iv)	(v)
O(4c)	x	−0.0733	0.0	−0.0733	−0.0733	−0.0733
	y	−0.0107	0.0	−0.0107	−0.0107	−0.0107
O(8d)	x	0.2257	0.2636	0.2121	0.2257	0.2257
	y	0.3014	0.2636	0.2879	0.3014	0.3014
	z	0.0385	0.0	0.0385	0.0385	0.0385
La(4c)	x	0.0063	0.0	0.0	0.0	0.0063
	y	0.5436	0.5	0.5	0.5	0.5435

$$|\tilde{\phi}_{n\mathbf{k}}\rangle = \sum_m (S^{-1/2})_{mn} |\phi_{m\mathbf{k}}\rangle, \tag{14}$$

where $S_{mn}=\langle\phi_{m\mathbf{k}}|\phi_{n\mathbf{k}}\rangle$. Since the Wannier functions obtained as Fourier transforms of the orbitals $|\tilde{\phi}_{n\mathbf{k}}\rangle$ are often already well localized, and furthermore allow to maximize a certain orbital character in the resulting Wannier function, the functions $|\tilde{\phi}_{n\mathbf{k}}\rangle$ have often been used without further minimization of the spread functional.[6,8,11,12]

Once a set of MLWFs is obtained, the corresponding Hamilton matrix, $\mathbf{H}^{(\mathrm{W})}(\mathbf{k})$, is constructed by a unitary transformation

$$\mathbf{H}^{(\mathrm{W})}(\mathbf{k}) = (\mathbf{U}^{(\mathbf{k})})^{\dagger}(\mathbf{U}^{\mathrm{dis}(\mathbf{k})})^{\dagger}\mathbf{H}^{(\mathrm{B})}(\mathbf{k})\mathbf{U}^{\mathrm{dis}(\mathbf{k})}\mathbf{U}^{(\mathbf{k})} \tag{15}$$

from the (diagonal) Hamilton matrix in the Bloch basis, $H^{(\mathrm{B})}_{nm}(\mathbf{k})=\varepsilon_{n\mathbf{k}}\delta_{nm}$, with eigenvalues $\varepsilon_{n\mathbf{k}}$. The MLWF Hamiltonian in real space is then calculated as a Fourier transform of $\mathbf{H}^{(\mathrm{W})}(\mathbf{k})$, which in practice is replaced by a sum over N_k points in $\mathbf{k}$ space

$$h^{\mathbf{T}}_{nm} = \frac{1}{N_k}\sum_{\mathbf{k}} e^{-\mathrm{i}\mathbf{k}\cdot\mathbf{T}} H^{(\mathrm{W})}_{nm}(\mathbf{k}). \tag{16}$$

Thus, the real space representation of the Hamiltonian in the MLWF basis is equivalent to a TB description of the full Hamiltonian within the corresponding orbital subspace

$$\hat{H} = \sum_{\mathbf{T},\Delta\mathbf{T}} h^{\Delta\mathbf{T}}_{nm}\hat{c}^{\dagger}_{n\mathbf{T}+\Delta\mathbf{T}}\hat{c}_{m\mathbf{T}} + \mathrm{H.c.}, \tag{17}$$

where $c_{m\mathbf{T}}$ is the annihilation operator for an electron in orbital $|w_{m\mathbf{T}}\rangle$. The real-space MLWF matrix elements $h^{\mathbf{T}}_{nm}$ can therefore be interpreted as hopping amplitudes within a TB picture of MLWFs [compare Eq. (17) with Eq. (2)]. Note that $\Delta\mathbf{T}$ in Eq. (17) refers to lattice vectors whereas $\Delta\mathbf{R}$ in Eq. (2) refers to Mn sites. The subscripts n and m in Eq. (17) can thus in general indicate both site and orbital/spin character (for cases with more than one site per unit cell).

For the case when MLWFs are constructed from an isolated set of bands, the TB model, Eq. (17), exactly reproduces the band dispersion within the corresponding energy window. For the entangled case, the energy bands calculated from Eq. (17) do not necessarily have to coincide with the underlying Bloch bands.

C. Structural decomposition

To analyze the effect of the various distinct structural distortions within the experimental *Pbnm* structure on the electronic properties of $LaMnO_3$ we investigate several different atomic configurations (similar to Ref. 25):

(i) The ideal cubic perovskite structure [Fig. 1i].

(ii) A purely JT-distorted structure [Fig. 1ii], which results from alternating long and short O-O distances within the x-y plane, i.e., a staggered JT distortion $Q^x_{\mathbf{R}}=\pm Q^x_0$ and $Q^z_{\mathbf{R}}=0$. This distortion doubles the unit cell within the x-y plane, leading to new in-plane lattice vectors $\mathbf{a}_{\mathrm{ii}}=a_{\mathrm{c}}(\hat{\mathbf{y}}+\hat{\mathbf{x}})$ and $\mathbf{b}_{\mathrm{ii}}=a_{\mathrm{c}}(\hat{\mathbf{y}}-\hat{\mathbf{x}})$ and tetragonal symmetry.

(iii) A purely GFO-distorted structure [Fig. 1iii], resulting from rotations of the oxygen octahedra around the z direction and octahedral tilts away from z, alternating along all three Cartesian directions. This distortion quadruples the unit cell compared to the undistorted structure (i), yielding orthorhombic *Pbnm* symmetry. The resulting in-plane lattice vectors are identical to those of structure (ii) and the new lattice vector along z is $\mathbf{c}_{\mathrm{iii}}=2a_{\mathrm{c}}\hat{\mathbf{z}}$.

(iv) A superposition of JT and GFO distortion, which also leads to orthorhombic *Pbnm* symmetry and unit-cell vectors unchanged with respect to structure (iii).

(v) The full experimental structure [Fig. 1v] with orthorhombically strained lattice vectors ($|\mathbf{a}_{\mathrm{v}}|\neq|\mathbf{b}_{\mathrm{v}}|\neq|\mathbf{c}_{\mathrm{v}}|$, resulting in $Q^z_{\mathbf{R}}\neq 0$) and displaced La cations compared to structure (iv).

For each of these structural modifications we use the same volume $V=60.91$ Å^3 per formula unit as in the experimentally observed *Pbnm* structure.[32] This leads to a cubic lattice parameter $a_{\mathrm{c}}=3.9345$ Å, which deviates only by 0.8% from the value we obtain by volume optimization for the ideal perovskite structure within GGA. For the positions of the O anions in structures (ii) and (iii) we use the same decomposition of structure (iv) into pure JT and GFO components as described in Ref. 25 (see Table I). For the cases with A-AFM order, the unit cell is doubled in z direction for both (i) and (ii) structures in order to accommodate the magnetic order, thus changing the symmetry to tetragonal in case (i).

Starting from the ideal cubic perovskite structure, we analyze the effect of a specific distortion by gradually increasing the amount of this distortion, i.e., we perform series of calculations using a linear superposition of the Wyckoff positions in the cubic perovskite structure and in structure (x)

$$\mathbf{R}(\alpha_x) = (1-\alpha_x)\mathbf{R}^{(\mathrm{i})} + \alpha_x \mathbf{R}^{(x)} \tag{18}$$

and vary α_x between 0 and 1. The following cases are considered: (x=ii) (pure JT distortion), (x=iii) (pure GFO distortion), and (x=iv) (combined JT and GFO distortions).

D. Computational details

We perform spin-polarized first-principles DFT calculations using the QUANTUM-ESPRESSO program package,[33] the GGA exchange-correlation functional of Perdew, Burke, and Ernzerhof,[34] and Vanderbilt ultrasoft pseudopotentials[35] in which the La($5s$,$5p$) and Mn($3s$,$3p$) semicore states are included in the valence.

Convergence has been tested for the total energy and total magnetization using the ideal cubic perovskite structure and ferromagnetic (FM) order. We find the total energy converged to an accuracy better than 1 mRy and the total magnetization converged to an accuracy of $0.05\mu_B$ for a plane-wave energy cutoff of 35 Ry and a Γ-centered $10\times10\times10$ k-point grid using a Gaussian broadening of 0.01 Ry. These values for plane-wave cutoff and Gaussian broadening are used in all calculations presented in this work. The $10\times10\times10$ k-point grid is used in all calculations for the cubic structure (i) whereas appropriately reduced k-point grids of $10\times10\times5$, $7\times7\times10$, and $7\times7\times5$ are used for the structures with unit cell doubled in the z direction, doubled in the x-y plane, and quadrupled, respectively.

After obtaining the DFT Bloch bands within GGA, we construct MLWFs using the WANNIER90 program integrated into the QUANTUM-ESPRESSO package.[36] Starting from an initial projection of atomic d basis functions $|3z^2-r^2\rangle$ and $|x^2-y^2\rangle$ centered at the different Mn sites within the unit cell onto the Bloch bands, we obtain a set of two e_g-like MLWFs per spin channel for each site. The spread functional (both gauge-invariant and nongauge-invariant parts) is considered to be converged if the corresponding fractional change between two successive iterations is smaller than 10^{-10}. For cases with entangled bands a suitable energy window is chosen as described in the corresponding "Results" section.

III. RESULTS AND DISCUSSION

A. Perfect cubic perovskite—structure (i)

The projected densities of states (DOS) and band structure calculated for $LaMnO_3$ in the ideal cubic perovskite structure (i) for both FM and A-AFM orders are shown in Fig. 2.[37]

A metallic state is obtained for both FM and A-AFM orders, in agreement with previous band-structure calculations.[25,29,30] The projected DOS show that the (local) majority spin bands around the Fermi energy have mainly Mn(e_g) character and are half-filled while the (local) minority spin bands with mainly Mn(e_g) character are unoccupied, as expected from the formal electron configuration. Bands with Mn(t_{2g}) character are lying just below the Mn(e_g) bands and slightly overlap with the latter. O(p) bands are located below the Mn(t_{2g}) bands (between ~6–12 eV) and are fully occupied. The strong hybridization between Mn(d) and O(p) electrons can be seen from the substantial amount of Mn(d) character in the energy range around 8 eV, i.e., toward the bottom of the bands with predominant O(p) character. The states above the Mn(e_g) bands have predominantly La(d) character.

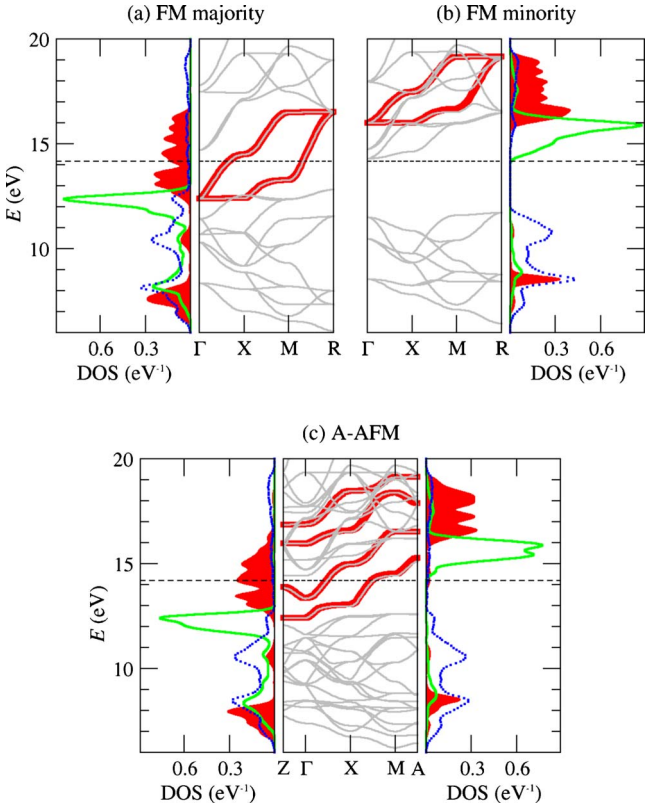

FIG. 2. (Color online) Projected DOS and band structure along high symmetry lines within the BZ calculated for the cubic structure (i) and both FM and A-AFM order. Filled (red) areas and solid (green) lines represent the projected DOS corresponding to Mn(e_g) and Mn(t_{2g}) states, respectively, while dashed (blue) lines represent the site and orbitally averaged projected DOS corresponding to the O p states. For the A-AFM case the left (right) panel corresponds to local majority (minority) spin projection. In the band structure plots, the dispersion calculated from the e_g-like MLWFs are represented by thick (red) lines, whereas the thin (gray) lines represent the DFT band structure. The Fermi level is indicated by the horizontal dashed lines.

One can see from the band structures depicted in Fig. 2 that for the FM majority spin channel the bands with predominant e_g character are nearly completely isolated from both higher- and lower-lying bands, while for the FM minority spin channel and in the A-AFM case, the "e_g bands" overlap strongly with other bands [with mostly Mn(t_{2g}) minority and La(d) character]. As described in Sec. II D, in order to construct e_g-like MLWFs for the various cases, we define an energy window for the disentanglement procedure [see Eq. (12)] and then initialize the Wannier functions from a projection of atomic e_g wave functions on the Kohn-Sham states within that energy window (see Ref. 19). A suitable energy window is chosen based on the e_g projected DOS and calculated band structure (see discussion below for more details). Two MLWFs per spin channel for the single Mn site

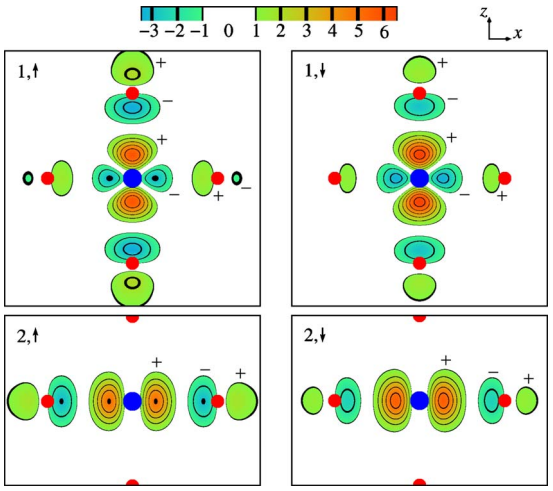

FIG. 3. (Color online) Real-space representation of the MLWFs for majority and minority spin projections in the cubic structure (i) with FM order, projected on the x-z plane passing through Mn (large/blue sphere) and O (small/red spheres) sites (in arbitrary units).

within the cubic unit cell are constructed for FM order, and two pairs of MLWFs, localized at the two Mn sites within the magnetic unit cell, are constructed for A-AFM order (for global spin-up projection only).

Figure 3 shows the real-space representation of the two e_g-like MLWFs for both majority and minority spin and FM order, calculated for an energy window of [12.0, 17.0] and [15.9, 20.0] eV, respectively. The shape of the MLWFs resembles the antibonding σ^* character of hybridization between Mn(e_g) and O(p) states in this energy range. The hybridization is notably stronger for the majority spin MLWFs (individual spread per WF 2.90 Å^2 compared to 1.65 Å^2 for the minority spin MLWFs), which is due to the smaller energy separation between the atomic Mn(e_g) and O(p) levels for the majority spin channel. The difference between the real-space representation of the MLWFs for FM and A-AFM order (not shown here) is more subtle. A quantitative comparison of the corresponding differences in the real-space Hamilton matrix elements between MLWFs will be presented below.

The dispersion calculated from the obtained e_g MLWFs is also shown in Fig. 2. It can be seen that even in the cases with strongly entangled e_g bands (FM minority spin and A-AFM) the MLWF bands follow certain DFT bands almost exactly, except around some band crossings with higher lying La d bands. This represents the fact that within cubic symmetry the e_g states cannot hybridize with the t_{2g} bands and hybridize only very weakly with the La d states.

In order to reproduce the two majority spin bands around the Fermi energy for the FM case, the lower bound of the energy window, $E_{\min}$, has to be above the lower peaks in the Mn(e_g) projected DOS at around 10.5 and 8 eV, which correspond to the bonding combination of hybridized atomic O(p) and Mn(e_g) states. If these bands are included in the energy window, the bonding and antibonding combinations of atomic orbitals become disentangled and the e_g Wannier functions become essentially "atomiclike" (compare also

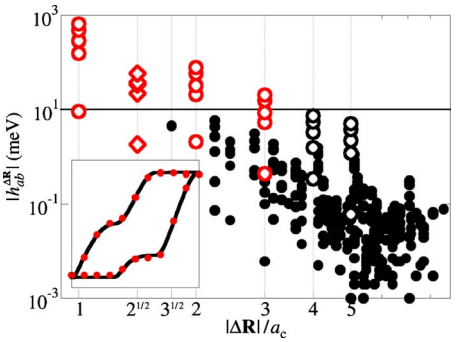

FIG. 4. (Color online) Magnitude of all calculated nonzero hopping parameters for FM order in the ideal cubic structure as a function of the intersite distance $|\Delta\mathbf{R}|$ (open circles: hopping along the unit cell directions; open diamonds: hopping between next-nearest neighbors; filled circles: all other hoppings). Inset: comparison of the full MLWF band structure (solid lines) and the one calculated from a simplified TB model (filled circles) which includes only the inter-site hoppings for which the largest matrix element is larger than 10 meV (see main text).

with the case of $SrVO_3$ described in Ref. 9). On the other hand, varying $E_{\min}$ within 0.4 eV below the Γ point energy of the e_g-like bands changes the MLWF bands by less than 1 meV for any $\mathbf{k}$. Similarly, varying the upper bound of the energy window has only minor influence on the resulting MLWF bands due to the negligible hybridization of the e_g states with higher-lying bands. Additional test calculations for different k-point grids showed that the MLWF band structure is converged within 0.5 meV at any k point for the $10\times10\times10$ grid which was used for the energy window test calculations.

We now turn to the analysis of the hopping parameters, i.e., the real-space matrix elements $h_{ab}^{\Delta\mathbf{R}}$, Eq. (16), between MLWFs located at different Mn sites. The magnitudes of all calculated hopping parameters for the FM majority spin case are shown in Fig. 4. It is noticeable that the hopping amplitudes along the three Cartesian axes are most dominant and that their decay with distance is rather slow so that the terms corresponding to intersite distances of $2a_c$ and $3a_c$ are of comparable magnitude as the hopping between next-nearest neighbors for which $|\Delta\mathbf{R}\rangle=\sqrt{2}a_c$.

The exact MLWF representation in terms of $\mathbf{H}^{(W)}(\mathbf{k})$ is well suited for further numerical calculations, e.g., within a DFT+DMFT approach. On the other hand, for the analysis of specific physical mechanisms within a semianalytical TB model, one generally wants to use only a very limited number of hopping parameters $\mathbf{h}^{\Delta\mathbf{R}}$ between closest neighbors. We therefore identify a minimal subset of hopping parameters, corresponding to intersite distances $|\Delta\mathbf{R}\rangle/a_c\in\{1,\sqrt{2},2,3\}$, i.e., where only hopping between sites, for which the leading term (i.e., the corresponding matrix element with largest magnitude) is larger than 10 meV, are considered, while the rest is set to zero. This model yields an overall very good agreement with the full MLWF band structure (see inset in Fig. 4), deviating not more than 0.11 eV for any k point on the $10\times10\times10$ k-point grid used. On the other hand, a TB model where only the hopping amplitudes between nearest and next-nearest neighbors are

TABLE II. Calculated values of the on-site, nearest-, and next-nearest-neighbor matrix elements $h_{ab}^{\Delta\mathbf{R}}$ (in meV) for FM and A-AFM order within structure (i) for the two different spin projections. As described in the text, in the A-AFM case all matrix elements refer to the Mn site closest to the origin.

	FM(↑)	FM(↓)	A-AFM(↑)	A-AFM(↓)
h_{11}^{0}	14485.7	17483.9	14638.9	17379.3
h_{22}^{0}	14484.3	17483.7	14541.7	17443.3
h_{11}^{z}	−648.2	−512.5	−595.0	−595.0
h_{22}^{z}	9.1	−9.2	−8.5	−8.5
h_{11}^{x}	−155.2	−135.0	−172.8	−130.7
h_{12}^{x}	284.5	217.9	281.4	214.5
h_{22}^{x}	−483.9	−386.7	−488.8	−389.8
h_{11}^{xz}	37.8	32.0	34.7	34.7
h_{12}^{xz}	−34.1	−26.6	−29.3	−29.0
h_{22}^{xz}	−1.8	1.2	0.5	0.5
h_{11}^{xy}	−21.9	−14.3	−16.4	−14.2
h_{22}^{xy}	57.9	47.4	51.4	48.3

taken into account leads to deviations of up to 0.29 eV for some k points, which might still be acceptable for certain purposes. However, the overall bandwidth for the latter model is reduced by about 0.2 eV compared to the full MLWF band structure.

The calculated matrix elements of the real-space matrix elements $h_{ab}^{\Delta\mathbf{R}}$ for nearest- and next-nearest neighbor hopping as well as the corresponding on-site terms ($\Delta\mathbf{R}=0$) are summarized in Table II. Here and in the following we use the abbreviated notation $\mathbf{h}^{z}$, corresponding to $\Delta\mathbf{R}=\pm a_c\hat{\mathbf{z}}$, and $\mathbf{h}^{xz}$, corresponding to $\Delta\mathbf{R}=a_c(\pm\hat{\mathbf{x}}\pm\hat{\mathbf{z}})$ (and analogously for all other Cartesian directions). We note that in the A-AFM case the translational equivalence between the two Mn sites within the unit cell is broken and $\Delta\mathbf{R}=\pm a_c\hat{\mathbf{z}}$ is not a lattice vector in this case. Nevertheless, in order to simplify the notation, we stick to the site-based index and note that for A-AFM order a translation along $\hat{\mathbf{z}}$ is equivalent to reversing the two spin projections. In the following we always report hopping amplitudes corresponding to hopping from and to the Mn site at the origin, the corresponding parameters for all other sites within the unit cell follow from symmetry. Similarly, we do not add a spin index to the MLWF matrix elements but instead discuss each case separately.

It can be seen that the hopping parameter between two $|3z^2-r^2\rangle$-like MLWFs along the z direction, h_{11}^{z} ($\equiv t$ in the effective model description), is the leading term for the nearest-neighbor hopping and that overall the next-nearest-neighbor hopping is about an order of magnitude smaller than the nearest-neighbor hopping. The hopping amplitude between two $|x^2-y^2\rangle$-like functions along the z direction, h_{22}^{z} ($\equiv t'$ in the model description), is indeed very small compared to h_{11}^{z}. In the FM case, all nearest-neighbor hopping amplitudes for the minority spin orbitals (except h_{22}^{z}) are reduced (to about 75–85 %) compared to the majority spin channel. This reflects the weaker hybridization between minority spin e_g and O($2p$) states, leading to more localized minority spin MLWFs with reduced hopping amplitudes. For A-AFM order, h_{11}^{z} corresponds to the hopping between a local majority and a local minority spin orbital, and its value, [92% of h_{11}^{z} for FM (↑)], is intermediate between the corresponding FM majority and minority values. The A-AFM hopping amplitudes within ferromagnetically ordered x-y planes for local majority/minority spin directions are very similar to the corresponding FM hoppings (differing by less than 5 meV), with the exception of the (local) majority spin h_{11}^{x} value, which is larger than that. Similar relations between the FM majority and minority spin and A-AFM values are also observed for the next-nearest-neighbor hoppings.

It can easily be verified, that the hopping parameters for FM majority and minority spin fulfill the relations described in Eqs. (3)–(5), as required for cubic symmetry. However, if the terms proportional to $t'\equiv h_{22}^{z}$ are neglected, the corresponding equations are not exactly fulfilled. Thus, simply neglecting h_{22}^{z} while keeping all other nearest-neighbor hopping amplitudes unchanged, leads to slight deviations from cubic symmetry. Furthermore, Eqs. (3)–(5) are clearly not fulfilled for the A-AFM hopping amplitudes, which reflects the overall tetragonal symmetry resulting from the magnetic order.

This symmetry reduction for the A-AFM case is also visible in the on-site matrix elements h_{11}^{0} and h_{22}^{0}, which differ by about 100 meV. On the other hand, the small asymmetry ($\sim$1 meV) in these on-site terms for FM order results from small numerical accuracies during the total spread minimization (which uses the full k-point grid so that cubic symmetry is not automatically enforced).

Within the effective two-band model for manganites described in Sec. II A, the Hund's rule coupling leads to an on-site spin splitting equal to $2J$ (treating $\mathbf{S_R}$ as classical unit vector). From the calculated on-site MLWF matrix elements, we thus obtain a value of $J=1.499$ eV for the Hund's rule coupling parameter in the FM case, and $J=1.370/1.451$ eV from the A-AFM on-site terms. The differences between these values indicate the limits of the assumption of a fixed t_{2g} core spin. We note that all these values are slightly larger than the results obtained in previous LSDA calculations ($J=1.34$ eV),[25] which reflects the fact that GGA in general leads to a stronger magnetic splitting than LSDA.[38,39]

Overall, the results obtained via MLWFs are in a very good qualitative agreement with the previous study using TB fits to DFT band structures.[25] However, the direct comparison between the values calculated from MLWF in this work and the values reported in Ref. 25 is slightly hampered by the different exchange correlation functionals and pseudopotentials used in the two studies. The same fitting method as described in Ref. 25 applied to the GGA band structure calculated in the present work, leads to a nearest-neighbor hopping parameter $t=-688$ meV, i.e., slightly larger than the −648 meV obtained from the MLWFs. This is due to the larger majority spin e_g bandwidth obtained here, $W_{\uparrow}=4.126$ eV, compared to the value of 3.928 eV reported in Ref. 25. Thus, the difference in bandwidth compensates the neglect of further neighbor hopping in the simple TB fit, leading to the apparent very good agreement between $h_{11}^{z}=-648$ meV listed in Table II and the corresponding value ($t=-655$ meV) given in Ref. 25.

In the following sections, we will analyze the influence of the structural distortions only for the on-site and nearest-

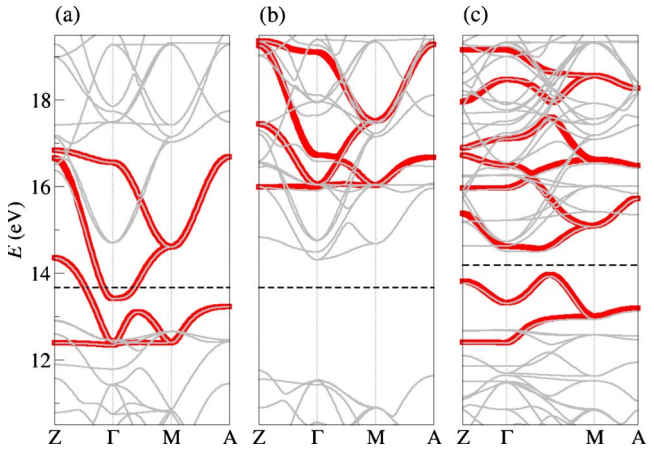

FIG. 5. (Color online) DFT band structure (thin lines) for the JT-distorted structure (ii): (a) majority spin FM, (b) minority spin FM, and (c) A-AFM. MLWF bands are depicted as thick/red lines. The Fermi level is indicated by the dashed line.

neighbor hopping terms. We have verified that the resulting changes in the further neighbor hopping amplitudes do not lead to significant differences in the dispersion characteristics of the e_g bands, even though the corresponding relative changes in the next-nearest neighbor hoppings are comparable with those of the nearest-neighbor hoppings.

B. Jahn-Teller distortion—structure (ii)

As described in Sec. II C, the staggered JT distortion, $Q^x_{\mathbf{R}} = \pm Q^x_0$, leads to a unit cell doubling within the x-y plane. In the case of FM order, we therefore construct two pairs of e_g MLWFs for each spin channel, localized at the two different Mn sites within the unit cell, while for A-AFM order we construct four pairs of MLWFs, localized at the four different Mn sites within the corresponding unit cell (for global spin-up projection only). The same approach for choosing the energy window for the disentanglement procedure was used as described in the previous section.

The calculated DFT band structure and e_g-like MLWF dispersion for the JT distorted structure (ii) are shown in Fig. 5. As a result of the unit-cell doubling, there are now four and eight bands with e_g character per spin channel for the FM and A-AFM order, respectively. As for the cubic perovskite structure, the calculated MLWF dispersion largely follows the DFT band structure, except where there is strong hybridization with states of a different orbital character. It can be seen that several degeneracies and potential band crossings, which would result from a simple "backfolding" of the cubic band structure onto the smaller tetragonal BZ, are lifted due to the JT distortion. This can be seen for example for the FM majority spin bands, where the highest-lying band along ΓZ acquires some dispersion, leading to a splitting of the higher energy e_g states at Z. Similarly, the degeneracy of the two lowest-lying e_g states at Γ is lifted, and a potential crossing of e_g bands is prevented between Γ and M. The latter splitting, together with the reduced dispersion along ΓZ for A-AFM order, appears crucial for the opening of an energy gap in the JT-distorted A-AFM ordered structure [Fig. 5(c)].

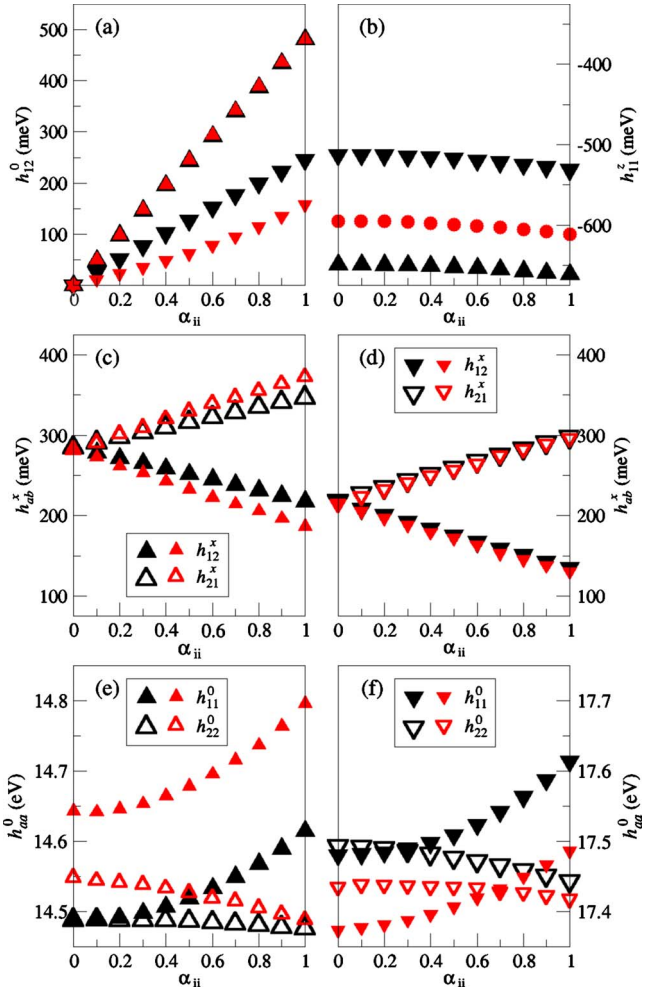

FIG. 6. (Color online) MLWF Hamiltonian matrix elements $h^{\Delta\mathbf{R}}_{ab}$ as function of the JT distortion. Large/black and small/red symbols correspond to FM and A-AFM order, respectively. Matrix elements associated with pure (local) majority and minority spin character are shown as triangles pointing up and down, respectively. Closed circles in (b) represent the A-AFM h^z_{11} hopping.

To further analyze the influence of the JT distortion on the e_g electronic structure, we perform a series of calculations where we gradually change the oxygen positions from the ideal perovskite structure (i) to the fully JT distorted structure (ii), according to Eq. (18), and monitor the resulting changes in the MLWF Hamiltonian matrix elements. In all these calculations, we use the same energy windows of [12.0, 17.5], [15.9, 20.0], and [12.0, 20.0] eV for the disentanglement in the case of FM majority, FM minority and A-AFM, respectively. The resulting MLWF matrix elements are depicted in Fig. 6. As discussed in the previous section, we report only hopping from and to the Mn site at the origin. The hopping amplitudes corresponding to other sites in the unit cell follow from symmetry. We find a strong linear dependence on the JT distortion for both the off-diagonal on-site matrix elements h^0_{12} [Fig. 6(a)] as well as for the off-diagonal in-plane hopping $h^x_{12/21}$ [Fig. 6(c) and 6(d)]. All other on-site and nearest-neighbor hopping matrix elements

show only a weak or moderate quadratic dependence on α_{ii}.

Within the model described in Sec. II A the sole effect of the JT distortion $(Q^x_{\mathbf{R}}, Q^z_{\mathbf{R}})$ is a linear coupling to the on-site terms at site $\mathbf{R}$ according to

$$\mathbf{t}^0 = \begin{pmatrix} e_0 - \lambda Q^z_{\mathbf{R}} & -\lambda Q^x_{\mathbf{R}} \\ -\lambda Q^x_{\mathbf{R}} & e_0 + \lambda Q^z_{\mathbf{R}} \end{pmatrix}. \tag{19}$$

In our case $Q^z_{\mathbf{R}}=0$ and $Q^x_{\mathbf{R}}= \pm \alpha_{ii} Q^x_0$; e_0 is the on-site energy of the e_g orbitals. It can be seen from Fig. 6(a) that the off-diagonal element h^0_{12} indeed shows a linear dependence on α, consistent with Eq. (19). The corresponding slope, $-\lambda Q^x_0 = 482$ meV, is nearly identical for the FM majority and A-AFM local majority spin elements, whereas it is significantly smaller for the (local) minority spin matrix elements ($-\lambda Q^x_0 = 246/155$ meV). This indicates that the JT splitting is also a ligand-field effect, i.e., it is mediated by hybridization with the surrounding oxygen orbitals, which, as pointed out previously, is stronger for the energetically lower majority spin states. The values for the JT coupling constant λ obtained from the data shown in Fig. 6(a) are 3.19 eV/Å, 1.63 eV/Å, and 1.02 eV/Å, for majority, FM minority, and A-AFM local minority spin states, respectively. We note that the value of λ obtained for majority spin is approximately a factor of two larger than the value obtained from the fitting procedure described in Ref. 25. As we will discuss in more detail below, the source for this discrepancy is the strong linear splitting observed for the off-diagonal in-plane nearest-neighbor hoppings $h^x_{12/21}$, which is induced by the JT distortion [see Fig. 6(c) and 6(d)].

This splitting between $h^x_{12/21}$ again results from the underlying hopping between atomic Mn(e_g) and O(p) states, which (in leading order) depends linearly on the Mn-O distance. Since this dependence will be different for the $|3z^2-r^2\rangle$ and $|x^2-y^2\rangle$ orbitals, it can easily be verified that the effective hopping across a combination of one long and one short Mn-O bond within the x-y plane between two different e_g orbitals will also depend linearly on the JT distortion whereas the effective hopping between the same type of e_g orbitals will show only a quadratic dependence. We have verified, by constructing atomiclike Wannier functions for both Mn(e_g) and O(p) orbitals (corresponding to larger energy windows), that indeed the dependence on the Mn-O distance is much stronger for the hopping amplitude between the $|3z^2-r^2\rangle$-type orbital and a neighboring O(p) orbital than for the corresponding $|x^2-y^2\rangle$-type hopping, consistent with the observed splitting in the effective hopping amplitudes $h^x_{12/21}$ shown in Fig. 6(c) and 6(d).

It can be verified within a TB model where the linear splitting between h^x_{12} and h^x_{21} (and analogously for the hopping along the y direction) is taken into account via one extra parameter derived from the MLWF data, that this splitting partially cancels the effect of the on-site JT term on the band dispersion. In particular, the JT-induced "gap" between the second and third e_g band between Γ and M is reduced by increasing the h^x_{12}/h^x_{21} splitting whereas it is enhanced by increasing the JT coupling strength λ. Thus, the band dispersion resulting from reduced λ and no splitting between h^x_{12} and h^x_{21} looks very similar to the one obtained from the MLWF parameters (i.e., including the spitting between $h^x_{12/21}$). This is the reason why the fitting of the DFT band structure on a TB model that does not incorporate a h^x_{12}/h^x_{21} splitting (see Ref. 25) leads to a smaller value of λ than the one obtained from the MLWF parameters. An interesting question arising from this is whether, despite the very similar band dispersion, the two different TB parameterizations would lead to noticeable differences in calculated ordering temperatures for the collective JT distortion. We note that values of $\lambda \approx 2.8$ eV/Å have been obtained in Refs. 11 and 23, which are only slightly smaller than the value we obtain from the majority spin MLWFs. This difference could be partially due to our use of GGA instead of LSDA. However, it is also clear from the above discussion that the effect of the JT distortion on the Kohn-Sham band structure goes beyond the simple local coupling described by Eq. (7). Therefore, a strong dependence of the local JT coupling strength from the employed fitting procedure has to be expected.

The differences between the off-diagonal in-plane hopping parameters induced by the JT distortion indicate changes in the MLWFs themselves, i.e., the JT distortion alters the basis set of a MLWF-based TB model. We note that this is an unavoidable result of the effective "two-band" picture and in fact indicates the limit of how realistic such an effective model can get. Strictly speaking, the definition of a distortion-independent basis set is only possible within a full d-p TB model, based on truly atomiclike functions. The JT distortion enhances the hybridization between atomic d and p orbitals along the short octahedral axis and reduces hybridization along the long axis, which will undoubtedly change the orbital character of the effective d-p-hybridized Wannier orbitals.

On the other hand, the minimization of the total quadratic spread does not necessarily guarantee that the resulting MLWFs exhibit a specific orbital character, and a splitting between h^x_{12} and h^x_{21} could, in principle, also result simply from a unitary mixing of purely $|3z^2-r^2\rangle$- and $|x^2-y^2\rangle$-type basis functions. In order to check whether (at least part of) the observed splitting is due to such a mixing of orbital character, we have applied a local unitary transformation between the two MLWFs on each site, and studied the resulting changes in the various hopping matrices. The corresponding analysis is presented in the appendix. In essence, we find that it is impossible to retrieve the "cubic symmetry," i.e., the form described in Eqs. (3)–(5) and (19), simultaneously for $\mathbf{h}^0$, $\mathbf{h}^z$, and $\mathbf{h}^x$, and that even though a transformation of one of these terms to the desired form is always possible, such a transformation will in general increase the corresponding deviations in the other two terms. We have also verified that even using the Wannier functions based on projecting pure $|3z^2-r^2\rangle$ and $|x^2-y^2\rangle$ orbitals on the Bloch functions without further minimization of the spread functional [see Eq. (14)] leads only to minor quantitative changes. In the following we therefore always present results obtained directly from the MLWFs, which do not depend on a particular choice of basis and are uniquely determined from the Kohn-Sham states within the specified energy window.

The leading hopping term in z direction, h^z_{11} [Fig. 6(b)], exhibits only a weak quadratic change as a function of α_{ii}. We also find a similar weak quadratic dependence on the JT

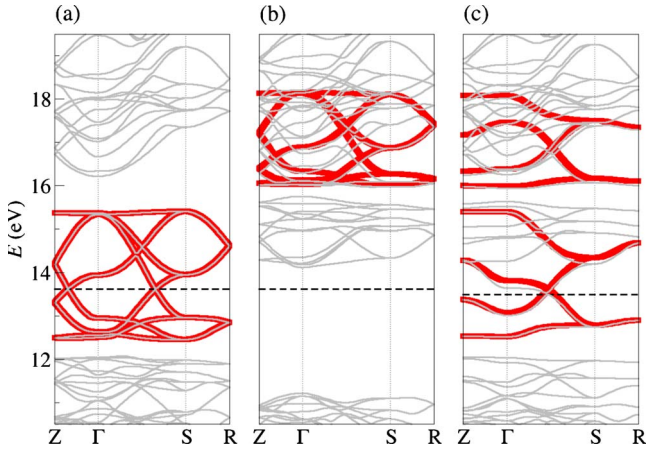

FIG. 7. (Color online) DFT band structure (thin lines) for the purely GFO-distorted structure (iii): (a) FM majority spin, (b) FM minority spin, and (c) A-AFM. MLWF bands are depicted as thick/red lines. The Fermi level is indicated by dashed lines.

distortion in the hopping parameters $h^x_{11/22}$ (not shown), and a moderately strong quadratic change in the on-site diagonal matrix elements [Fig. 6(e) and 6(f)], which introduces a splitting of about 150 meV between h^0_{11} and h^0_{22} for the fully JT distorted structure.

Finally, we note that the Hund's rule coupling parameters derived from the local spin splitting between MLWFs obtained for the fully JT-distorted structure ($J=1.499/1.484$ eV for FM order and $J=1.345/1.465$ eV for A-AFM order) are not significantly changed compared with the ones obtained for structure (i).

C. $GdFeO_3$-type distortion—structure (iii)

The band dispersion calculated for the purely GFO-distorted structure (iii) is presented in Fig. 7. The rotation and tilting of oxygen octahedra in structure (iii) distorts the ideal 180° Mn-O-Mn bond angle, which is expected to reduce the hopping amplitudes. Indeed, it can be seen in Fig. 7 that the GFO distortion leads to significantly smaller bandwidth [2.951 eV and 2.139 eV for FM majority and minority spin, respectively, compared to 4.126 eV and 3.156 eV in the undistorted structure (i)]. As a result, the FM majority spin e_g bands become completely separated from the lower-lying t_{2g} bands and the La(d) bands at higher energy. Unlike in the JT distorted structure (ii), the system stays metallic for both FM and A-AFM order.

Since the unit cell for structure (iii) is quadrupled with respect to the cubic perovskite structure, there are now eight bands with dominant e_g character for each spin direction. However, due to the tilt/rotation of the oxygen octahedra, "e_g-like" orbitals at a certain site can hybridize with "t_{2g}-like" orbitals at a neighboring site, leading to bands with mixed e_g/t_{2g} character.[40] In the FM case this does not represent a problem for the disentanglement procedure since the bands with predominant e_g character are separated from the predominantly t_{2g} bands for both spin direction. For FM order, we can therefore construct four pairs of MLWFs, localized at the four different sites within the unit cell, by defining appropriate energy windows separately for each spin direction. This is not possible in the A-AFM case, where the local minority t_{2g} bands overlap strongly with the local majority e_g bands in the energy region between 14 and 16 eV. In this case, the standard disentanglement procedure employed for structures (i) and (ii), i.e., defining an energy window [12.0, 21.0] eV and initializing eight Wannier functions from projections on atomic e_g orbitals at the various sites, results in MLWFs with mixed t_{2g}/e_g orbital character. In particular, the resulting local minority spin MLWFs exhibit a rather strong t_{2g} character.

A possible way to overcome this problem would be to construct all 20 d-like MLWFs (5 per Mn site), i.e., both e_g and t_{2g} orbitals. However, the resulting MLWFs still contain some amount of e_g/t_{2g} mixing, and the corresponding MLWF matrix elements exhibit systematic deviations from the results obtained in the previous sections, which are derived from a smaller set of MLWFs. In the following, we therefore adopt a different strategy to obtain model parameters for the A-AFM case, and construct the four local majority and four local minority spin e_g-like MLWFs separately, using two different energy windows. From this, we obtain the on-site matrix elements $\mathbf{h}^0$ as well as the hopping parameters $\mathbf{h}^x$ within the x-y plane (and of course all further neighbor hopping amplitudes within this plane). On the other hand we do not obtain the hopping amplitudes $\mathbf{h}^z$ between adjacent planes in the z direction, which would connect the two separate sets of MLWFs. Similar to the purely JT distorted case, we analyze the effect of the GFO distortion on the e_g bands by performing calculations with varying degree of distortion, i.e., by changing the oxygen positions according to Eq. (18). In this case we always adjust the energy window for the construction of the MLWFs to the actual e_g bandwidth corresponding to a particular α_{iii}. We note that the use of projector-based Wannier functions according to Eq. (14), i.e., without quadratic spread minimization, would face similar technical problems, depending on whether the projected orbitals are oriented relative to the global crystal axes or according to the orientation of the local oxygen octahedron.

We find that the main effect of the GFO distortion is indeed a systematic reduction of all hopping amplitudes by $\approx 20-30\%$, consistent with what was reported in Ref. 25. However the construction of MLWFs allows to analyze this result in more detail. Figure 8(a) shows the overall reduction for all obtained nearest-neighbor hopping amplitudes for both FM and A-AFM order while Fig. 8(b) resolves the reduction factors of the various hopping amplitudes for full GFO distortion ($\alpha_{\mathrm{iii}}=1$). It can be seen, that even though there is a significant spread in the reduction factors for the various hopping parameters, the overall reduction can approximately be described as $\mathbf{h}^{x/z}(\alpha_{\mathrm{iii}})=\mathbf{h}^{x/z}(0)(1-\eta\alpha^2_{\mathrm{iii}})$, with an average value of $\eta=0.26$.

In addition to the changes in the nearest-neighbor hopping amplitudes, we also observe a quadratic decrease in the on-site diagonal matrix elements as a function of the GFO distortion [Fig. 8(c) and 8(d)] with a similar magnitude for both orbitals and different magnetic order. This can be understood again from the underlying hopping between atomic p and d orbitals. Since the effective e_g bands correspond to the antibonding combination of these atomic orbitals, a reduction in

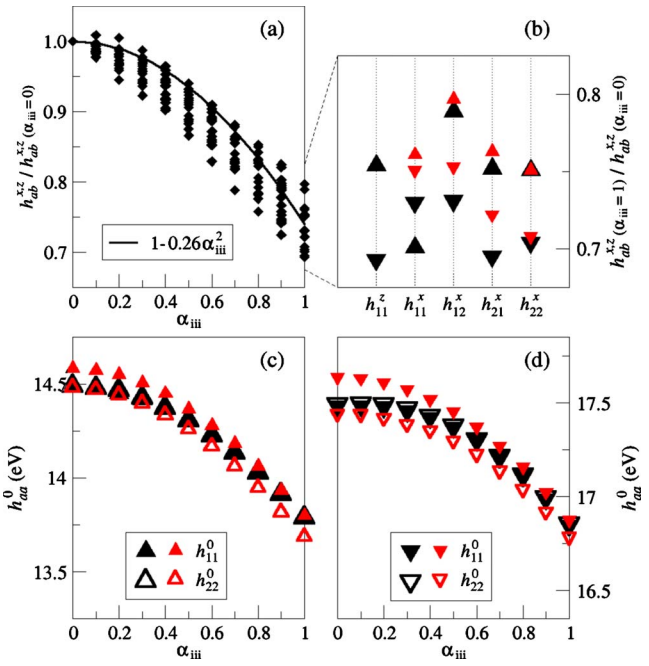

FIG. 8. (Color online) Hamiltonian matrix elements in the basis of MLWFs as a function of the GFO distortion. Large/black and small/red symbols correspond to FM and A-AFM order, respectively. Elements associated with purely (local) majority and minority spin characters are represented by triangles pointing up and down, respectively.

the underlying *p*-*d* hopping amplitudes results in a decrease in the Γ-point energy of the e_g states. The Hund's rule coupling parameter $J=1.502$ eV obtained from the on-site splitting for FM order and $\alpha_{\mathrm{iii}}=1$ is very similar to the corresponding value for the cubic perovskite structure.

D. Combined Jahn-Teller and $GdFeO_3$-type distortion—structure (iv)

So far we have analyzed the individual effects of the JT and GFO distortion. We now discuss whether the superposition of both distortions gives rise to any changes in the MLWF matrix elements that go beyond a simple superposition of the individual effects. The corresponding band structure and MLWF dispersion for structure (iv), i.e., the combined JT and GFO distortion, is presented in Fig. 9. It can be seen that the band structure in this case closely resembles the one of the purely GFO distorted structure (iii), Fig. 7, but with the additional JT-induced effects (avoided band crossings and lifted degeneracies) as described in Sec. III B. Note that, as in the purely JT-distorted structure, the FM case is metallic, whereas a band gap opens only for A-AFM order.

As described in the previous section we construct eight MLWFs per spin direction for the FM case and two separate sets of four local majority and four local minority e_g-like MLWFs for the A-AFM case. Figure 10 shows the evolution of selected MLWF matrix elements as a function of distortion. The atomic positions are changed according to Eq. (18) with x=iv. By comparing Fig. 10(a) with Fig. 6(a), it can be seen that the GFO distortion does also significantly reduce

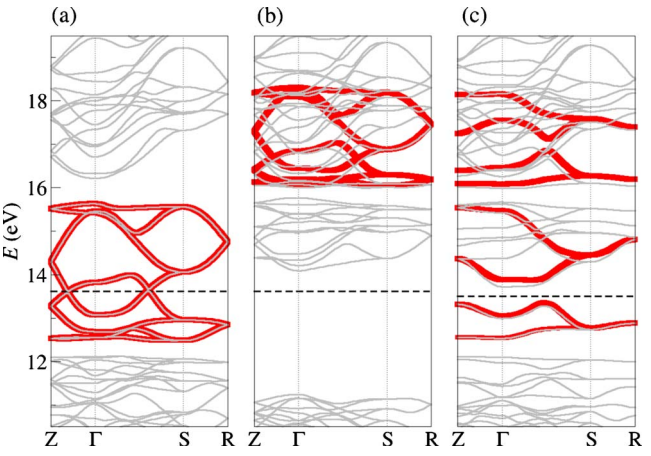

FIG. 9. (Color online) DFT band structure (thin lines) for structure (iv): (a) majority spin FM, (b) minority spin FM, and (c) A-AFM. MLWF are depicted as thick/red lines. Fermi level is indicated by dashed line.

the on-site matrix elements h^0_{12} (to ≈75–80%), which are otherwise proportional to the JT distortion. This is further evidence for the ligand-field nature of the JT coupling, i.e., that it is mediated by the Mn-O hybridization (which is reduced by the GFO distortion). Furthermore, it can be seen that the leading hopping along z, h^z_{11}, follows very closely the trend observed for the purely GFO distorted structures. In the case of the off-diagonal hopping amplitudes within the *x*-*y* plane, the superposition of GFO-distortion-induced reduction and JT-induced splitting leads to an initial increase in

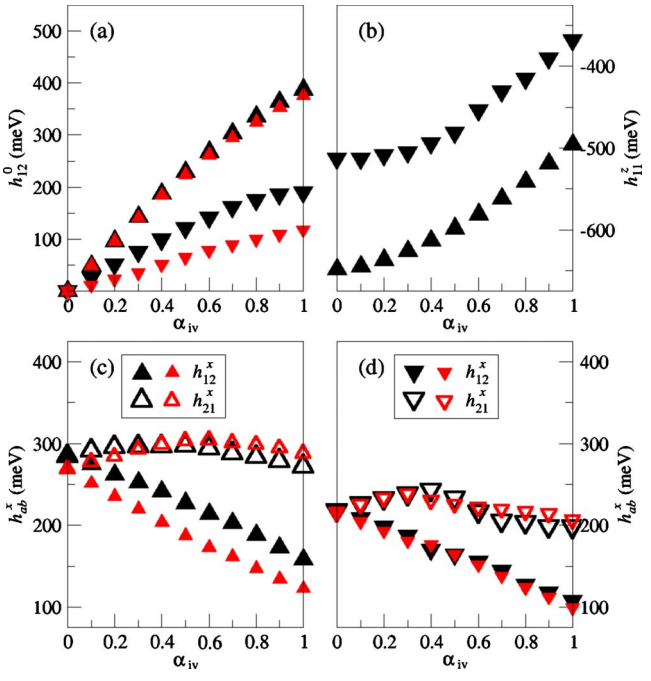

FIG. 10. (Color online) MLWF Hamiltonian matrix elements as function of combined JT and GFO distortion. Large/black and small/red symbols correspond to the FM and A-AFM order, respectively. Elements associated with purely (local) majority and minority spin characters are represented by triangles pointing up and down, respectively.

h_{12}^{x} for small distortion, followed by a decrease for larger α_{iv}. Overall, the observed trends can indeed be well understood as independent superposition of the individual effects of JT and GFO distortions. We note that the kinks observed in some of the minority spin hopping terms around $\alpha_{\mathrm{iv}} \approx 0.4$ result from the opening of the gap between e_g-like and t_{2g}-like minority spin bands for this amount of distortion, which represents a certain "discontinuity" for the disentanglement procedure. Nevertheless, it can be seen that the resulting MLWFs allow to observe a clear trend even for cases with very strongly entangled bands and a symmetry that allows mixing between many different orbital characters.

E. Simplified TB models for $LaMnO_3$ in the full experimental *Pbnm*—structure (v)

The analysis presented so far showed that the effect of different structural distortions on the e_g bands can, to a good extent, be treated independently of each other. In this section, we attempt to incorporate the most significant effects described in the previous sections into a refined effective TB model. Then, in order to test the accuracy of the resulting parameterization, we compare the resulting band dispersion with the full GGA and MLWF band structure, calculated for the full experimental *Pbnm* structure of $LaMnO_3$ and A-AFM order, as well as with the A-AFM MLWF band structure for all other structural configurations discussed previously. This allows us to clearly identify which simplifications have the largest overall effect on the band dispersion and how they can be remedied, if desirable.

For the refined TB model we introduce different hopping amplitudes for local majority/minority spin projections to describe the hopping between ferromagnetically aligned nearest neighbors within the x-y planes ($t^{\uparrow\uparrow}/t^{\downarrow\downarrow}$), and an intermediate value for the nearest neighbor hopping between antiferromagnetically aligned nearest neighbors along the z direction ($t^{\uparrow\downarrow}$), i.e., hopping between two different local spin projections. This is in accordance with our results presented in Sec. III A. For the corresponding hopping amplitudes we use the values of h_{11}^{z} calculated for the ideal cubic perovskite structure (see Table II) for FM and A-AFM order, which are then reduced by the same factor $(1-\eta\alpha_{\mathrm{iii}}^{2})$, where α_{iii} describes the amount of pure GFO distortion. Apart from these modifications we assume the usual cubic symmetry of the nearest-neighbor hopping matrices, i.e.,

$$\mathbf{t}^{ss'}(\pm a_{\mathrm{c}}\hat{\mathbf{z}}) = (1-\eta\alpha_{\mathrm{iii}}^{2})t^{ss'}\begin{pmatrix}1 & 0\\ 0 & 0\end{pmatrix}, \tag{20}$$

$$\mathbf{t}^{ss'}(\pm a_{\mathrm{c}}\hat{\mathbf{x}}) = (1-\eta\alpha_{\mathrm{iii}}^{2})t^{ss'}\begin{pmatrix}\frac{1}{4} & -\frac{\sqrt{3}}{4}\\ -\frac{\sqrt{3}}{4} & \frac{3}{4}\end{pmatrix} \tag{21}$$

[and analogously for $\mathbf{t}^{ss'}(\pm a_{\mathrm{c}}\hat{\mathbf{y}})$]. Note that s and s' in these equations should be read as a *local* spin index, i.e., it designates the spin projection relative to the orientation of the local core spin. We use the average value $\eta=0.26$ determined in Sec. III C.

The JT-induced splitting of the nondiagonal elements of the hopping matrix within the x-y plane discussed in Sec. III B is incorporated in the TB model as an additional contribution to the in-plane hopping

$$\Delta\mathbf{t}(\pm a_{\mathrm{c}}\hat{\mathbf{x}}) = \tilde{\lambda}Q_0^{x}\alpha_{\mathrm{ii}}(1-\eta\alpha_{\mathrm{iii}})\begin{pmatrix}0 & 1\\ -1 & 0\end{pmatrix} \tag{22}$$

[and analogously for $\Delta\mathbf{t}(\pm a_{\mathrm{c}}\hat{\mathbf{y}})$]. Here, α_{ii} describes the amplitude of the staggered JT distortion, i.e., $Q_{\mathbf{R}}^{x}=\pm Q_0^{x}\alpha_{\mathrm{ii}}$, and the parameter $\tilde{\lambda}$ is determined from the average splitting over all hopping amplitudes in the purely JT-distorted structure [shown in Fig. 6(c) and 6(d)]. In addition, we include the usual on-site JT effect in essentially the same form as described in Eq. (7) but with a spin-dependent JT coupling constant that is also reduced by the GFO distortion (with the same factor as the hopping amplitudes)

$$\lambda \rightarrow \lambda^{s}(1-\eta\alpha_{\mathrm{iii}}^{2}). \tag{23}$$

We note that the orthorhombic strain in the experimental structure of $LaMnO_3$ gives rise to a homogeneous Q^z component to the JT distortion, i.e., the same $Q_{\mathbf{R}}^{z}\neq 0$ on all sites, which we take into account within the model by using the same coupling constant λ^s as for the Q^x component.

We also include hopping between next-nearest neighbors and between second nearest neighbors along the Cartesian coordinate axes in the refined TB model but we do not consider any spin dependence of the corresponding hopping amplitudes. We describe the hopping between next-nearest neighbors by spin-independent parameters t^{xy} corresponding to the hopping between two $|3z^2-r^2\rangle$-type orbitals along the $\pm a_{\mathrm{c}}\hat{\mathbf{x}}\pm a_{\mathrm{c}}\hat{\mathbf{y}}$ directions. The parameter t^{xy} is taken as spin average over the corresponding MLWF matrix elements h_{11}^{xy} calculated for the cubic structure. All other hopping matrix elements between next-nearest neighbors are determined from this via the following relations, which are derived assuming cubic symmetry and indirect hopping only (see Ref. 25):

$$\mathbf{t}^{xz} = t^{xy}(1-\eta\alpha_{\mathrm{iii}}^{2})\begin{pmatrix}-2 & \sqrt{3}\\ \sqrt{3} & 0\end{pmatrix}, \tag{24}$$

$$\mathbf{t}^{xy} = t^{xy}(1-\eta\alpha_{\mathrm{iii}}^{2})\begin{pmatrix}1 & 0\\ 0 & -3\end{pmatrix}. \tag{25}$$

The same GFO-distortion-induced reduction as for the nearest-neighbor hopping matrices is applied. The hopping between second nearest neighbors along the coordinate axes $[\mathbf{t}(\pm 2a_{\mathrm{c}}\hat{\mathbf{x}}),\mathbf{t}(\pm 2a_{\mathrm{c}}\hat{\mathbf{y}}),\mathbf{t}(\pm 2a_{\mathrm{c}}\hat{\mathbf{z}})]$ is included according to the ideal cubic symmetry relations described by Eqs. (3)–(5), with a_{c} replaced by $2a_{\mathrm{c}}$, $t'=0$, and $t=t^{2z}$, where t^{2z} is estimated from the MLWF matrix elements for the purely GFO distorted structure. We note that the reduction of this parameter compared to the undistorted case is significantly stronger than for the nearest (and next-nearest) neighbor hopping amplitudes. Furthermore, the hopping between third nearest neighbors along the coordinate axes $[\mathbf{t}(\pm 3a_{\mathrm{c}}\hat{\mathbf{x}}),\mathbf{t}(\pm 3a_{\mathrm{c}}\hat{\mathbf{y}}),\mathbf{t}(\pm 3a_{\mathrm{c}}\hat{\mathbf{z}})]$, that was considered in Sec. III A, becomes negligible as result of the GFO distortion.

TABLE III. Parameters used in the TB models.

	Refined	Simple
$t^{\uparrow\uparrow}$ (eV)	−0.648	−0.492
$t^{\downarrow\downarrow}$ (eV)	−0.512	−0.492
$t^{\uparrow\downarrow}$ (eV)	−0.569	−0.492
η	0.26	
$\tilde{\lambda}$ (eV Å^{-1})	0.53	0
$\lambda^{\uparrow}$ (eV Å^{-1})	3.19	1.64
$\lambda^{\downarrow}$ (eV Å^{-1})	1.33	1.64
t^{xy} (eV)	−0.018	0
t^{2z} (eV)	−0.020	0
e_0 (eV)	15.356	15.505
J (eV)	1.5	1.805

Finally, we include the Hund's rule coupling in the refined TB model using the standard form [Eq. (6)] with an average value of J obtained from the MLWF on-site splitting. In order to relate the obtained TB bands to the full GGA and MLWF band structures, we determine the on-site energy e_0 as the spin and orbital average of the corresponding h^0_{aa} matrix elements for the A-AFM experimental structure.

The values of all parameters used in the refined TB model are summarized in Table III. The JT distortion in the experimental *Pbnm* structure corresponds to $\alpha_{\rm ii}=1$, $Q^x_0=-0.161$ Å, and $Q^z=-0.048$ Å, and the corresponding amplitude of the GFO distortion is $\alpha_{\rm iii}=1$.

We also compare with a very simple TB model that includes only nearest-neighbor hopping according to Eqs. (3)–(5) with $t'=0$, and the standard JT and Hund's rule coupling as described by Eqs. (7) and (6). The parameters for this model are chosen via typical simplified fitting procedures: the nearest-neighbor hopping parameter $-t$ is obtained as one sixth of the majority spin bandwidth W for the fully GFO distorted structure (iii) and FM order; the JT coupling constant λ is taken from Ref. 25, where it was obtained by fitting a similar TB model (including also next-nearest-neighbor hopping) to a DFT band structure; J is calculated from the spin splitting between FM majority and minority bands at the Γ point for the cubic structure (i); and e_0 is fitted such that the Fermi energy is aligned with the DFT calculation value.

Figure 11(a) shows the band dispersion obtained from the GGA calculation for the full experimental structure (v) and A-AFM order as well as the corresponding MLWF bands. Figures 11(b) and 11(c) show the comparison between the MLWF bands and the two different simplified TB models. It can be seen that the orthorhombic lattice strain and La displacements do not lead to significant qualitative changes in the band structure as compared to structure (iv) [see Fig. 9(c)]. The comparison between the MLWF dispersion and the refined TB model [Fig. 11(b)] shows that, despite the many simplifications made, this model reproduces the MLWF bands to a remarkable accuracy. The only major discrepancy can be seen for the lowest-lying local minority band along Γ-Z at $E\sim 16$ eV, which is slightly lower than the corresponding MLWF band. This can be traced back to

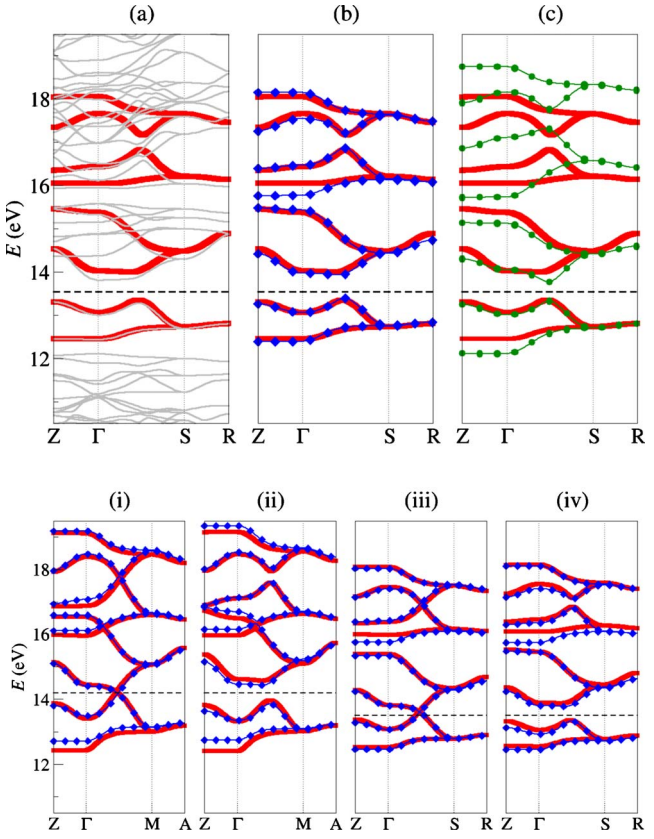

FIG. 11. (Color online) Top: (a) DFT bands (thin/gray lines) and MLWF bands (thick/red lines) for the A-AFM experimental *Pbnm* structure (v). (b) Comparison of the MLWF bands with the refined TB model and (c) with the simple nearest-neighbor TB model. Bottom: comparison between MLWF bands (thick/red lines) and refined TB model (thin lines with diamonds) for structures (i)–(iv) and A-AFM order. The Fermi level is indicated by dashed lines.

an overestimation of the minority spin h^x_{22} hopping, which results from the fact that we use the same reduction factor η for all hoppings. As can be seen in Fig. 8(b), the corresponding hopping amplitude is affected more strongly by the GFO distortion than any other nearest neighbor hopping (for A-AFM order). The very simple nearest-neighbor TB model depicted in Fig. 11(c) deviates much stronger from the MLWF band structure than the refined model but still captures the overall dispersion surprisingly well. Consistent with our analysis from the previous sections, the deviations are more pronounced for the energetically higher local minority spin bands, which is clearly due to the neglected spin dependence of the hopping. As discussed in Sec. III B, the smaller JT coupling constant used in the simple model partially cancels the missing effect of the JT distortion on the interorbital in-plane hopping parameters, leading to the relative good agreement of the simpler model with the MLWF bands around the Fermi level.

In Figs. 11(i)–(iv), we also verify the validity of the refined TB model for all previously discussed structures (i)–(iv) and A-AFM order. It can be seen that the overall agreement between MLWFs and the refined model is very good. The most pronounced deviations are due to the already mentioned features: underestimated t^{2z} hopping used for

structures (i) and (ii), and overestimated minority spin h_{22}^{x} used for structures (iii) and (iv). The same trends are also observed for the FM majority and minority bands (not shown). In summary, the maximum deviation between MLWFs and refined TB bands in all cases is in the range (250 ± 150) meV, while the k-point averaged deviation is in the range of only (70 ± 50) meV.

IV. SUMMARY AND CONCLUSIONS

We have shown that the construction of maximally localized Wannier functions together with the disentanglement procedure described in Ref. 19 can be used to extract effective e_g bands in $LaMnO_3$ even for cases where these bands are strongly entangled with other states. This procedure thus provides a very robust way for extracting the "correlated subspace" used for example in DFT+DMFT calculations.

We have used this procedure to obtain a TB parameterization of the e_g bands for different structural modifications of $LaMnO_3$ with both FM and A-AFM order. By monitoring the effect of the individual distortions on the MLWF matrix elements, we can assess the quality of the various approximations and simplifications that are commonly used in model Hamiltonians for manganite systems (using the GGA Kohn-Sham band structure as reference for the noninteracting part of the Hamiltonian). In particular, we find the following:

(a) while the nearest-neighbor hopping is clearly dominant, the further neighbor hopping along the Cartesian axes decays rather slowly. Taking into account nearest, next-nearest, as well as second and third nearest hopping along the Cartesian axes leads to deviations of less than 0.11 eV from the (cubic FM) DFT band structure.

(b) In addition to the linear on-site coupling to the JT distortion, we observe a strong effect on the in-plane hopping amplitudes between different orbitals. The corresponding splitting, which is due to the underlying Mn-O hopping, partially cancels the effect of the on-site term on the band dispersion, which has a strong influence on the determination of the local JT coupling strength.

(c) The GFO distortion leads to an overall reduction in all hopping amplitudes by about 25–30 % and also reduces the local JT splitting. This reduction is due to the weaker hybridization between Mn(e_g) and O(p) states for non-180° bond angle.

(d) The higher energy of the (local) minority spin states reduces the hybridization between the corresponding atomic e_g and O(p) states, leading to reduced hopping amplitudes and JT coupling compared to the majority spin states.

(e) The splitting between (local) majority and minority spin states is generally well described by the local Hund's rule coupling, even though small variations in the corresponding J values indicate the limits of the core spin approximation.

It is apparent that the most crucial deviations from the simple two band description are a result of the underlying Mn-O hybridization. Nevertheless, we have shown that a refined TB model that incorporates the effects described above using the parameters listed in Table III reproduces the DFT band structure calculated for the full experimental crystal structure of $LaMnO_3$ with remarkable accuracy. Whether this accuracy, at the prize of more parameters in the model, is desirable depends of course on the specific application of the model description.

Furthermore, our analysis shows that the effects of the various distinct structural distortions present in $LaMnO_3$ are (to a good approximation) independent from each other and can therefore be assessed individually. However, the GFO distortion has to be taken into account to obtain the correct magnitude of the Jahn-Teller coupling.

In comparison with the manual TB fits presented in Ref. 25, the direct construction of Wannier functions is less biased and more universally applicable. It allows to *calculate* parameters of the model instead of *fitting* them to either experimental or computational data. In particular, it is possible to obtain very accurate TB representations even for rather complex band structures. While in this study we have used MLWFs, we note that other choices of the unitary transformation matrices in Eqs. (10) and (12) have also been used.[6,8,11,12] Whether MLWFs, projector-based Wannier functions, or other schemes are preferable might depend on the specific case. To the best of our knowledge no systematic comparison for a number of "difficult" cases (i.e., with strongly entangled band structures and low symmetry) has been performed so far. For the specific case described in the appendix only small differences between MLWFs and projector-based Wannier functions have been observed.

The TB representation obtained from MLWFs (or other schemes) includes hopping to all further neighbors and by construction gives an *exact* representation of the underlying band structure (at least for the case of an isolated set of bands). On the other hand for certain purposes it might be desirable to use a much more simplified model, for example with hopping only between nearest neighbors. Using the corresponding hopping parameters obtained from MLWFs for such a model (and essentially neglecting all the corresponding further neighbor hoppings), would lead to a significant underestimation of the total e_g bandwidth. In such a case it might be desirable to use nearest-neighbor hopping amplitudes that lead to a realistic bandwidth instead of the ones obtained from the MLWFs. In essence, care has to be applied when parameters corresponding to a more complex parameterization are used for simpler models. The analysis presented in this work demonstrates that, depending on the specific application at hand, MLWFs can in principle be used to construct more and more refined TB parameterizations which lead to realistic, materials-specific band structures with very high accuracy.

ACKNOWLEDGMENTS

This work was supported by Science Foundation Ireland under Reference No. SFI-07/YI2/I1051 and made use of computational facilities provided by the Trinity Center for High Performance Computing.

APPENDIX A: LOCAL UNITARY TRANSFORMATION OF MLWFS FOR PURELY JT-DISTORTED STRUCTURE (II)

As pointed out in Sec. III B, the observed JT-induced splitting in the off-diagonal in-plane hopping amplitudes

$h^x_{12/21}$ can, in principle, also result from a simple mixing between the $|3z^2-r^2\rangle$ and $|x^2-y^2\rangle$ orbital character in the MLWFs. Even though the initial Wannier functions used as starting point for the localization procedure are obtained by projecting the corresponding atomic e_g orbitals onto the Kohn-Sham states, it is not guaranteed that the final MLWFs still exhibit the same orbital character. In order to investigate whether at least some of this orbital character can be retained by a simple local mixing between the two MLWFs corresponding to a particular Mn site **R**, we apply the following unitary transformation:

$$\mathbf{U}(\theta_\mathbf{R}) = \begin{pmatrix} \cos\theta_\mathbf{R} & \sin\theta_\mathbf{R} \\ -\sin\theta_\mathbf{R} & \cos\theta_\mathbf{R} \end{pmatrix}. \tag{A1}$$

A unitary transformation can always be found such that either $\mathbf{h}^0$, $\mathbf{h}^z$, or $\mathbf{h}^x$ have the form corresponding to an ideal $|3z^2-r^2\rangle/|x^2-y^2\rangle$ basis [see Eqs. (3), (4), and (19)]. The corresponding conditions for these three cases are: (a) $h^0_{11}(\theta_0)=h^0_{22}(\theta_0)$, (b) $h^z_{12}(\theta_z)=0$, and (c) $h^x_{12}(\theta_x)=h^x_{21}(\theta_x)$.

Note that due to the staggered JT distortion with $Q^x_\mathbf{R}=\pm Q^x_0$ the corresponding local transformation angles will exhibit the same pattern as the local JT distortion, i.e., $\theta_\mathbf{R}=\pm\theta$. This leads to the following transformations for the above mentioned MLWF matrices:

$$\mathbf{h}^{0/z}(\theta) = \mathbf{U}^\dagger(\theta)\mathbf{h}^{0/z}\mathbf{U}(\theta), \tag{A2}$$

$$\mathbf{h}^{x}(\theta) = \mathbf{U}^\dagger(-\theta)\mathbf{h}^{x}\mathbf{U}(\theta) \tag{A3}$$

and the following special transformation angles:

$$\theta_0 = \frac{1}{2}\arctan[(h^0_{11}-h^0_{22})/(2h^0_{12})], \tag{A4}$$

$$\theta_z = \frac{1}{2}\arctan[(2h^z_{12})/(h^z_{22}-h^z_{11})], \tag{A5}$$

$$\theta_x = \frac{1}{2}\arctan[(h^x_{21}-h^x_{12})/(h^x_{11}+h^x_{22})], \tag{A6}$$

which yield the specific "cubic" forms of the $\mathbf{h}^0$, $\mathbf{h}^z$ and $\mathbf{h}^x$ matrices, respectively. It is clear from the results presented in Sec. III B that for nonzero JT distortion one finds $\theta_0\neq\theta_x\neq\theta_z$.

The deviation of $\mathbf{h}^{\Delta\mathbf{R}}$ from their cubic forms (for $\Delta\mathbf{R}$ corresponding to "0," "z," and "x") can be expressed as

$$\Delta h^0_{11/22} = \mp h^0_\mathrm{A}\sin[2(\theta-\theta_0)], \tag{A7}$$

$$\Delta h^z_{12} = -h^z_\mathrm{A}\sin[2(\theta-\theta_z)], \tag{A8}$$

$$\Delta h^x_{12/21} = \mp h^x_\mathrm{A}\sin[2(\theta-\theta_x)], \tag{A9}$$

where the amplitudes $h^{\Delta\mathbf{R}}_\mathrm{A}$ are defined as

$$h^{0/z}_\mathrm{A} = \frac{1}{2}\sqrt{(h^{0/z}_{11}-h^{0/z}_{22})^2+(2h^{0/z}_{12})^2}, \tag{A10}$$

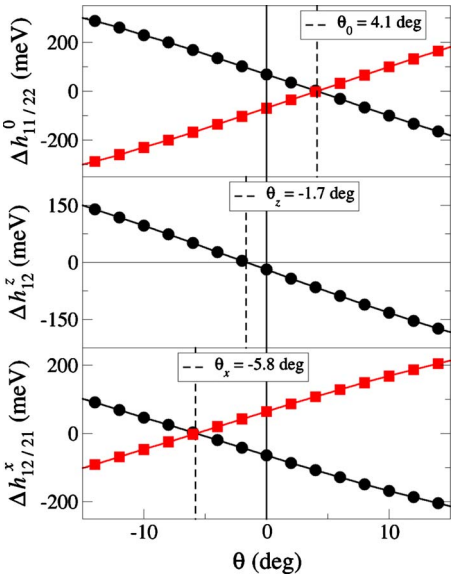

FIG. 12. (Color online) Deviations $\Delta h^{\Delta\mathbf{R}}_{ab}$ of the selected matrix elements from the cubiclike form as a function of the transformation angle θ. Vanishing deviations (and the corresponding angles θ_0, θ_z, and θ_x) are marked by vertical dashed lines.

$$h^x_\mathrm{A} = \frac{1}{2}\sqrt{(h^x_{12}-h^x_{21})^2+(h^x_{11}+h^x_{22})^2}. \tag{A11}$$

Figure 12 shows the quantities $\Delta h^0_{11/22}$, Δh^z_{12}, and $\Delta h^x_{12/21}$ defined in Eqs. (A7)–(A9) as functions of the transformation angle θ. Note that $\theta=0$ corresponds to the matrix elements as obtained directly from the maximum localization procedure, i.e., with $h^0_{11/22}$ and $h^x_{12/21}$ split and an essentially negligible deviation of h^z_{12} from 0. It is apparent that transforming the MLWFs by either θ_0, θ_z, or θ_x (indicated by vertical dashed line), will always enhance the deviation from cubic symmetry for one (or both) of the three considered matrices. There is no "optimal" transformation which would retain the cubic $|3z^2-r^2\rangle/|x^2-y^2\rangle$ symmetry of the basis set, which shows that the JT distortion inevitably leads to changes in hybridization between atomic Mn(e_g) and O(p) states.

Table IV compares the transformation angles θ_0, θ_z, and θ_x obtained from the MLWFs with the corresponding angles obtained for projector-type Wannier functions according to Eq. (14). As discussed in Sec. II B these Wannier functions are taken as initial guess for the unitary matrices $\mathbf{U}^{(\mathbf{k})}$ and $\mathbf{U}^{\mathrm{dis}(\mathbf{k})}$, and have previously been used (without subsequent spread minimization) within DFT+DMFT calculations and to obtain model Hamiltonian parameters.[6,8,11,12] It can be seen that the deviations from the cubic orbital character rep-

TABLE IV. Comparison between the transformation angles θ_0, θ_z, and θ_x obtained for MLWFs and for projector-type Wannier functions according to Eq. (14).

	θ_0 (deg)	θ_z (deg)	θ_x (deg)
MLWFs	4.1	−1.7	−5.8
Projected	0.7	−4.9	−2.5

resented by these angles are slightly different for the two types of Wannier functions but that they are of rather similar magnitude. On average, the deviations are slightly smaller for the projected Wannier functions compared to the MLWFs, i.e., the $|3z^2-r^2\rangle/|x^2-y^2\rangle$ orbital symmetry is probably slightly better retained for the projected Wannier functions than for the MLWFs. However, it is also clear that the absolute differences between the two types of Wannier functions are small and that the projected Wannier functions also deviate form the ideal orbital symmetry [which, as discussed in Sec. III B, is an unavoidable result of the change in the underlying $O(p)-Mn(e_g)$ hybridization]. We note that the exact results for the projected Wannier functions will in general depend on the specific choice of the atomic orbital $|g_m\rangle$ (i.e., its radial part) whereas the MLWFs are completely basis-set independent. In view of this, and the fact that the maximal localization procedure (with $\theta=0$) seems to retain the cubic orbital character in the MLWFs to a quite reasonable degree, we believe that MLWFs are indeed a suitable tool for the analysis presented in this work. As can be seen in Fig. 6, the resulting changes in the effective model parameters are gradual and systematic, leading to well-reproducible trends. Nevertheless, other construction methods, such as the projector-based method, can be used as well, and might be equally well-suited.

*kovacikr@tcd.ie

[1] M. Imada, A. Fujimori, and Y. Tokura, Rev. Mod. Phys. **70**, 1039 (1998).
[2] E. Dagotto, T. Hotta, and A. Moreo, Phys. Rep. **344**, 1 (2001).
[3] S. Maekawa, T. Tohyama, S. E. Barnes, S. Ishihara, W. Koshibae, and G. Khaliullin, *Physics of Transition Metal Oxides* (Springer, New York, 2004).
[4] C. Lin and A. J. Millis, Phys. Rev. B **78**, 174419 (2008).
[5] T. F. A. Müller, V. Anisimov, T. M. Rice, I. Dasgupta, and T. Saha-Dasgupta, Phys. Rev. B **57**, R12655 (1998).
[6] W. Ku, H. Rosner, W. E. Pickett, and R. T. Scalettar, Phys. Rev. Lett. **89**, 167204 (2002).
[7] E. Pavarini, A. Yamasaki, J. Nuss, and O. K. Andersen, New J. Phys. **7**, 188 (2005).
[8] V. I. Anisimov *et al.*, Phys. Rev. B **71**, 125119 (2005).
[9] F. Lechermann, A. Georges, A. Poteryaev, S. Biermann, M. Posternak, A. Yamasaki, and O. K. Andersen, Phys. Rev. B **74**, 125120 (2006).
[10] I. V. Solovyev, Phys. Rev. B **73**, 155117 (2006).
[11] W.-G. Yin, D. Volja, and W. Ku, Phys. Rev. Lett. **96**, 116405 (2006).
[12] B. Amadon, F. Lechermann, A. Georges, F. Jollet, T. O. Wehling, and A. I. Lichtenstein, Phys. Rev. B **77**, 205112 (2008).
[13] R. O. Jones and O. Gunnarsson, Rev. Mod. Phys. **61**, 689 (1989).
[14] R. M. Martin, *Electronic Structure* (Cambridge University Press, Cambridge, 2004).
[15] A. Georges, G. Kotliar, W. Krauth, and M. J. Rozenberg, Rev. Mod. Phys. **68**, 13 (1996).
[16] V. I. Anisimov, A. I. Potaryaev, M. A. Korotin, A. O. Anokhin, and G. Kotliar, J. Phys.: Condens. Matter **9**, 7359 (1997).
[17] G. Kotliar and D. Vollhardt, Phys. Today **57**(3), 53 (2004).
[18] N. Marzari and D. Vanderbilt, Phys. Rev. B **56**, 12847 (1997).
[19] I. Souza, N. Marzari, and D. Vanderbilt, Phys. Rev. B **65**, 035109 (2001).
[20] T. Miyake and F. Aryasetiawan, Phys. Rev. B **77**, 085122 (2008).
[21] O. K. Andersen and T. Saha-Dasgupta, Phys. Rev. B **62**, R16219 (2000).
[22] E. Zurek, O. Jepsen, and O. K. Andersen, ChemPhysChem **6**, 1934 (2005).
[23] Z. Popovic and S. Satpathy, Phys. Rev. Lett. **84**, 1603 (2000).
[24] K. H. Ahn and A. J. Millis, Phys. Rev. B **61**, 13545 (2000).
[25] C. Ederer, C. Lin, and A. J. Millis, Phys. Rev. B **76**, 155105 (2007).
[26] K. Momma and F. Izumi, J. Appl. Crystallogr. **41**, 653 (2008).
[27] E. O. Wollan and W. C. Koehler, Phys. Rev. **100**, 545 (1955).
[28] J. B. A. A. Elemans, B. Van Laar, K. R. Van der Veen, and B. O. Loopstra, J. Solid State Chem. **3**, 238 (1971).
[29] W. E. Pickett and D. J. Singh, Phys. Rev. B **53**, 1146 (1996).
[30] S. Satpathy, Z. S. Popović, and F. R. Vukajlović, Phys. Rev. Lett. **76**, 960 (1996).
[31] V. I. Anisimov, F. Aryasetiawan, and A. I. Liechtenstein, J. Phys.: Condens. Matter **9**, 767 (1997).
[32] P. Norby, I. K. Andersen, E. K. Andersen, and N. Andersen, J. Solid State Chem. **119**, 191 (1995).
[33] P. Giannozzi *et al.*, J. Phys.: Condens. Matter **21**, 395502 (2009).
[34] J. P. Perdew, K. Burke, and M. Ernzerhof, Phys. Rev. Lett. **77**, 3865 (1996).
[35] D. Vanderbilt, Phys. Rev. B **41**, 7892 (1990).
[36] A. A. Mostofi, J. R. Yates, Y.-S. Lee, I. Souza, D. Vanderbilt, and N. Marzari, Comput. Phys. Commun. **178**, 685 (2008).
[37] Here and in the following we use the notation of Ref. 41 to denote special k points.
[38] D. J. Singh and J. Ashkenazi, Phys. Rev. B **46**, 11570 (1992).
[39] F. Lechermann, F. Welsch, C. Elsässer, C. Ederer, M. Fähnle, J. M. Sanchez, and B. Meyer, Phys. Rev. B **65**, 132104 (2002).
[40] Note that we are generally referring to $|3z^3-r^2\rangle$ and $|x^2-y^2\rangle$ as e_g orbitals and to all other d orbitals as t_{2g} orbitals, even in cases where, strictly speaking, these are not the correct symmetry labels.
[41] C. J. Bradley and A. P. Cracknell, *The Mathematical Theory of Symmetry in Solids* (Oxford University Press, Oxford, 1972).